

Theory of quasiparticle scattering interference on the surface of topological superconductors

Johannes S. Hofmann,^{1,2} Raquel Queiroz,¹ and Andreas P. Schnyder^{1,*}

¹Max-Planck-Institut für Festkörperforschung, Heisenbergstrasse 1, D-70569 Stuttgart, Germany

²Institut für Theoretische Physik und Astrophysik, Universität Würzburg, Am Hubland, D-97074 Würzburg, Germany

(Dated: May 23, 2022)

Topological superconductors, such as noncentrosymmetric superconductors with strong spin-orbit coupling, exhibit protected zero-energy surface states, which possess an intricate helical spin structure. We show that this nontrivial spin character of the surface states can be tested experimentally from the absence of certain backscattering processes in Fourier-transform scanning tunneling measurements. A detailed theoretical analysis is given of the quasiparticle scattering interference on the surface of both nodal and fully gapped topological superconductors with different crystal point-group symmetries. We determine the universal features in the interference patterns resulting from magnetic and nonmagnetic scattering processes of the surface quasiparticles. It is shown that Fourier-transform scanning tunneling spectroscopy allows us to uniquely distinguish among different types of topological surface states, such as zero-energy flat bands, arc surface states, and helical Majorana modes, which in turn provides valuable information on the spin and orbital pairing symmetry of the bulk superconducting state.

PACS numbers: 03.65.vf, 74.50.+r, 74.20.Rp, 74.25.F-

I. INTRODUCTION

An important class of materials for topological superconductivity are noncentrosymmetric superconductors (NCSs).¹ Both fully gapped and nodal NCSs can exhibit nontrivial topological characteristics manifested by surface states in the form of helical Majorana modes, arc surface states, or zero-energy surface flat bands.²⁻¹⁵ The stability of each of these three types of surface states is ensured by the conservation of a different bulk topological invariant. Interestingly, due to strong spin-orbit interactions, topological surface states of NCSs are strongly spin polarized and possess a highly unusual helical spin texture, where the spin direction varies as a function of surface momentum.¹⁶⁻²⁰

Due to time-reversal invariance, surface quasiparticles with opposite momenta have opposite spin polarizations. This in turn leads to the absence of elastic backscattering from nonmagnetic impurities, since scattering processes involving spin flips are forbidden unless time-reversal symmetry is broken. The absence of backscattering can be tested experimentally using Fourier-transform scanning tunneling spectroscopy (FT-STS).²¹⁻²⁵ This experimental technique uses the presence of dilute impurities to probe the electronic properties of surface quasiparticles at finite momenta \mathbf{q} through the analysis of interference patterns formed by impurity scattering processes.

In this paper, we present an analytical derivation and numerical simulations of the quasiparticle interference (QPI) on the surface of both nodal and fully gapped topological superconductors. For concreteness, we focus on single-band centrosymmetric and noncentrosymmetric superconductors, although our results can be generalized in a straightforward manner to any time-reversal invariant topological superconductor, e.g., to multiband superconductors with dominant spin-triplet pairing. The surface states of fully gapped topological superconductors are dispersing helical Majorana modes,^{2-5,16-20} whereas nodal topological superconductors without a center of inversion exhibit zero-energy surface flat bands,^{4,8-12} and depending on the crystal point-group symme-

try, may also support zero-energy arc surface states,^{8,12,16} see Fig. 1. We study the QPI patterns for these three types of topological surface states in the presence of magnetic and nonmagnetic impurities, and identify the universal features in the ordinary and spin-resolved FT-STS response that distinguish among the three types of surface states.

Interestingly, for helical Majorana modes and arc surface states, we find that the ordinary QPI patterns resulting from nonmagnetic impurities are weak and nonsingular, which is in line with the expected absence of elastic backscattering. Similarly, in the case of the flat-band surface states, the absence of backscattering suppresses the non-spin-resolved FT-STS signal produced by nonmagnetic scattering processes connecting states with opposite momentum signs. Magnetic impurities, on the other hand, give rise to a strong and divergent signal in the spin-resolved FT-STS for all three types of surface states. In the case of the helical Majorana modes, the divergent QPI patterns exhibit inverse square-root singularities at the momenta $|\mathbf{q}_{\parallel,0}| = 2E/\Delta_t$, whereas for the arc surface states, the divergences in the FT-STS response at $|q_{x,0}| = 2E/\Delta_t$ show a $1/q_x$ dependence.

The remainder of the paper is organized as follows. We begin in Sec. II with a phenomenological description of time-reversal invariant topological superconductors and their surface states. This is followed in Sec. III by an analytical derivation and numerical simulations of the QPI patterns. Our summary and conclusions are presented in Sec. IV. Some technical details are given in the Appendices.

II. NCS AND THEIR SURFACE STATES

Over the past few years, superconductivity has been discovered in many noncentrosymmetric compounds,¹ for example, in $\text{Li}_2\text{Pd}_x\text{Pt}_{3-x}\text{B}$,^{26,27} $\text{Mo}_3\text{Al}_2\text{C}$,^{28,29} and BiPd ,^{30,31} and in the heavy-fermion systems CePt_3Si ,³² CeIrSi_3 ,³³ and CeRhSi_3 .³⁴ The lack of bulk inversion symmetry in these materials generates strong Rashba-type spin-orbit couplings (SOCs) and

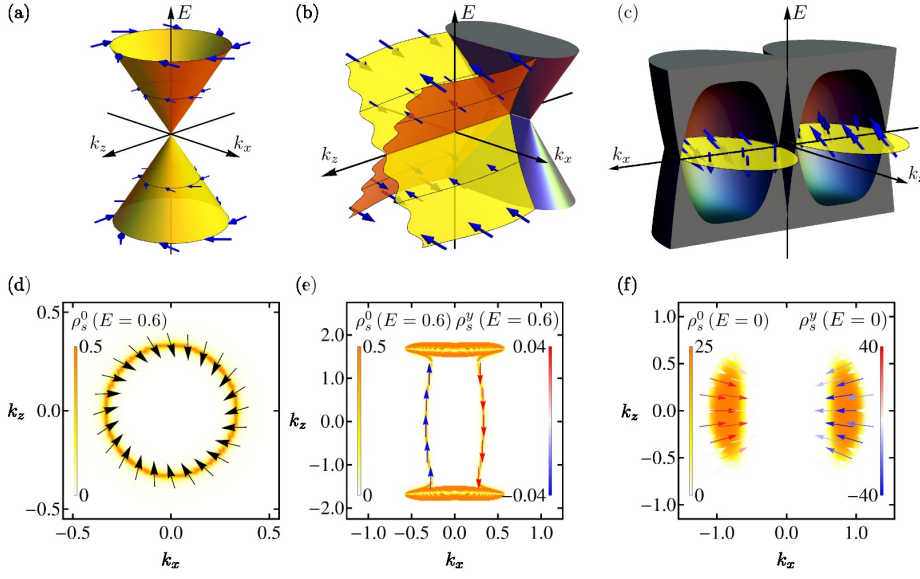


FIG. 1. (Color online) Energy spectrum and spin texture $\rho_s^\alpha(E, \mathbf{k}_\parallel)$ of the helical Majorana mode [(a) and (d)] and the arc state [(b) and (e)] on the (010) surface of a topological superconductor with point groups O and C_{4v} , respectively [cf. Eq. (1)]. Here we set $\lambda = -2.0$ and $\Delta_s = 0.5$. The arrows on the surface states indicated the magnitude and direction of the spin polarization. (c) and (f): Spin texture $\rho_s^\alpha(E = 0, \mathbf{k}_\parallel)$ of the zero-energy flat bands on the surface of a nodal NCS with point group C_2 , $\lambda = 0.5$, and $\Delta_s = 4.0$. In-plane and out-of-plane components of the spin polarization are represented in (f) by arrows and by color scale, respectively.

allows for a mixing of spin-singlet and spin-triplet pairing states. Due to these properties, many of the noncentrosymmetric superconductors are likely to exhibit unconventional pairing symmetries with nontrivial topological characteristics.

A. Model definition

We consider a generic phenomenological description of single-band NCSs given in terms of the Bogoliubov-de Gennes (BdG) Hamiltonian $\mathcal{H} = \frac{1}{2} \sum_{\mathbf{k}} \Psi_{\mathbf{k}}^\dagger H_{\mathbf{k}} \Psi_{\mathbf{k}}$, with $\Psi_{\mathbf{k}} = (c_{\mathbf{k}\uparrow}, c_{\mathbf{k}\downarrow}, c_{-\mathbf{k}\uparrow}^\dagger, c_{-\mathbf{k}\downarrow}^\dagger)^T$ the Nambu spinor and

$$H_{\mathbf{k}} = \begin{pmatrix} \varepsilon_{\mathbf{k}} \sigma_0 + \lambda \mathbf{l}_{\mathbf{k}} \cdot \boldsymbol{\sigma} & \Delta_{\mathbf{k}} \\ \Delta_{\mathbf{k}}^\dagger & -\varepsilon_{\mathbf{k}} \sigma_0 + \lambda \mathbf{l}_{\mathbf{k}} \cdot \boldsymbol{\sigma}^* \end{pmatrix}. \quad (1a)$$

Here, $c_{\mathbf{k}\sigma}^\dagger$ denotes the electron creation operator with spin σ and momentum \mathbf{k} , and $\boldsymbol{\sigma} = (\sigma_1, \sigma_2, \sigma_3)$ is the vector of Pauli matrices. The normal part of the Hamiltonian describes a three-dimensional cubic lattice with nearest-neighbor hopping t and chemical potential μ , $\varepsilon_{\mathbf{k}} = t(\cos k_x + \cos k_y + \cos k_z) - \mu$, and antisymmetric Rashba-type SOC $\lambda \mathbf{l}_{\mathbf{k}} \cdot \boldsymbol{\sigma}$ with SOC strength λ . The superconducting order parameter $\Delta_{\mathbf{k}}$ contains both even-parity spin-singlet and odd-parity spin-triplet components with

$$\Delta_{\mathbf{k}} = (\Delta_s \sigma_0 + \Delta_t \mathbf{d}_{\mathbf{k}} \cdot \boldsymbol{\sigma})(i\sigma_2), \quad (1b)$$

where Δ_s and Δ_t represent the spin-singlet and spin-triplet pairing amplitudes, respectively. In the absence of interband pairing, the superconducting transition temperature is maximized when the spin-triplet pairing vector $\mathbf{d}_{\mathbf{k}}$ is aligned with the SOC vector $\mathbf{l}_{\mathbf{k}}$.³⁵ Hence we assume that $\mathbf{d}_{\mathbf{k}} = \mathbf{l}_{\mathbf{k}}$. Unless stated otherwise, we set $(t, \mu, \lambda, \Delta_s, \Delta_t) = (4.0, 8.0, -2.0, 0.5, 2.0)$ for our numerical calculations and study the QPI patterns as a function of different types of SOC potentials. Since the spin polarization of the surface states is generic to NCSs and the absence of nonmagnetic backscattering is a consequence of time-reversal symmetry, different

values for the parameters $(t, \mu, \lambda, \Delta_s, \Delta_t)$ do not qualitatively alter our results.

Crystal lattice symmetries constrain the specific form of the SOC vector $\mathbf{l}_{\mathbf{k}}$.³⁶ Within a tight-binding expansion, we find that the lowest-order symmetry allowed term for the cubic crystallographic point group O , relevant for $\text{Li}_2\text{Pd}_x\text{Pt}_{3-x}\text{B}$ and $\text{Mo}_3\text{Al}_2\text{C}$, is given by

$$\mathbf{l}_{\mathbf{k}} = \sin k_x \hat{\mathbf{x}} + \sin k_y \hat{\mathbf{y}} + \sin k_z \hat{\mathbf{z}}. \quad (2a)$$

Similarly, for the tetragonal point group C_{4v} , experimentally represented by CePt_3Si , CeIrSi_3 , and CeRhSi_3 , we obtain

$$\mathbf{l}_{\mathbf{k}} = \sin k_y \hat{\mathbf{x}} - \sin k_x \hat{\mathbf{y}}. \quad (2b)$$

Finally, we also consider the monoclinic point group C_2 , relevant for BiPd , in which case the SOC vector $\mathbf{l}_{\mathbf{k}}$ takes the form

$$\mathbf{l}_{\mathbf{k}} = (\sin k_x + \sin k_y)(\hat{\mathbf{x}} + \hat{\mathbf{y}}) + \sin k_z \hat{\mathbf{z}}. \quad (2c)$$

B. Topological surface states

We first discuss the dispersion and spin polarization of the subgap states that appear at the surface of a topological superconductor described by the lattice BdG Hamiltonian (1). As a result of the strong SOC and the nontrivial topology of the bulk wave functions, these surface states possess an intricate helical spin texture. This is shown in Fig. 1, which displays the spin-, momentum-, and energy-resolved surface density of states,

$$\rho_s^\alpha(E, \mathbf{k}_\parallel) = -\frac{\hbar}{4\pi} \text{Im} \sum_{n=1}^{n_0} \text{Tr} \left\{ S^\alpha G_{nn}^{(0)}(E, \mathbf{k}_\parallel) \right\}. \quad (3)$$

Here, $G_{nn}^{(0)}(E, \mathbf{k}_\parallel) = [E + i\eta - H_{nn}(\mathbf{k}_\parallel)]^{-1}$ is the zero-temperature Green's function of Hamiltonian (1) in a slab geometry with surface perpendicular to the y axis, $H_{nn'}(\mathbf{k}_\parallel) = \frac{1}{2\pi} \int dk_y e^{ik_y(n-n')} H_{\mathbf{k}}$, $\mathbf{k}_\parallel = (k_x, k_z)$ denotes the surface

momentum, and $S^\alpha = (S^0, S^\mu)$ stands for the charge and spin operators in Nambu space with

$$S^\alpha = (\sigma_3 \otimes \sigma_0, \sigma_3 \otimes \sigma_1, \sigma_0 \otimes \sigma_2, \sigma_3 \otimes \sigma_3), \quad (4)$$

where $\alpha \in \{0, 1, 2, 3\}$. Unless indicated otherwise, we evaluate in the following expression (3) for a slab of thickness $N = 10^2$ using an intrinsic broadening of $\eta = 0.005$. The sum in Eq. (3) is taken over the first $n_0 = 10$ layers, which corresponds approximately to the decay length of the surface states. It was recently shown that, depending on the pairing symmetry, fully gapped or nodal topological superconductors of the form of Eq. (1) can support three different types of zero-energy surface states.¹²

a. Helical Majorana modes. Fully gapped time-reversal invariant topological superconductors with dominant triplet pairing exhibit linearly dispersing helical Majorana modes [see Fig. 1(a)].^{5,16,37} Similar to the surface states of topological insulators,^{38,39} the linearly dispersing Majorana modes of topological superconductors exhibit a helical spin texture, with the spin and momentum directions locked to each other. Interestingly, the spin of the helical Majorana mode is polarized entirely in the surface plane at all energies.

b. Arc surface states. Nodal NCSs with $\Delta_t > \Delta_s$ and l-vector given by Eq. (2b) support arc surface states,^{1,2,8,16-18} i.e., zero-energy states forming one-dimensional open arcs in the surface Brillouin zone, connecting the projections of two nodal rings of the bulk gap [Fig. 1(b)]. We find that the arc states show a strong spin polarization in the yz spin-plane, with a vanishing component along the x axis.

c. Zero-energy flat bands. Zero-energy flat bands generically occur at the surface of three-dimensional nodal NCSs whose triplet pairing component is comparable or larger than the singlet one.^{4,8,12} These flat-band surface states appear within regions of the surface Brillouin zone that are bounded by the projections of the bulk nodal lines [Fig. 1(c)]. Strong SOC together with the nontrivial bulk topology lead to an intricate three-dimensional spin-texture of the flat-band surface states, as indicated by the arrows and color scale in Fig. 1(c).

III. QPI OF TOPOLOGICAL SURFACE STATES

Weak and dilute scattering potentials on the surface of topological superconductors modulate the local density of states of the surface quasiparticles, thereby leading to quasiparticle scattering interference. Measurements of these interference patterns through FT-STs allow the study of the surface-state dispersion and polarization at finite momentum \mathbf{q} . In the following, the T -matrix formalism in Born approximation is employed to calculate the QPI spectra of subgap states on the (010) surface of topological superconductors. We consider both nonmagnetic and magnetic impurities described by

$$H_{\text{imp}}^\beta = \sum_{\mathbf{k}, \mathbf{q}} \Psi_{\mathbf{k}}^\dagger V_{\mathbf{q}}^\beta \Psi_{\mathbf{k}+\mathbf{q}}, \quad \text{with } V_{\mathbf{q}}^\beta = v_{\mathbf{q}} S^\beta, \quad (5)$$

where $V_{\mathbf{q}}^{\beta=0}$ corresponds to nonmagnetic disorder, whereas $V_{\mathbf{q}}^{\beta=1,2,3}$ represents isotropic magnetic exchange scattering

caused by impurity spins. For simplicity, we assume that the magnetic impurities are all fully polarized along the β spin axis by a small external magnetic field of strength $H \ll H_{c2}$. With this, the ordinary ($\alpha = 0$) and spin-resolved ($\alpha = 1, 2, 3$) FT-STs response $\delta\rho_s^{\alpha\beta}$, which is to a good approximation proportional to the Fourier-transformed differential conductance tensor dI_α/dV , is given by^{22,23}

$$\delta\rho_s^{\alpha\beta}(E, \mathbf{q}_{\parallel}) = -\frac{1}{2\pi i} \left[\Lambda^{\alpha\beta}(E, \mathbf{q}_{\parallel}) - \{ \Lambda^{\alpha\beta}(E, -\mathbf{q}_{\parallel}) \}^* \right], \quad (6)$$

with $\mathbf{q}_{\parallel} = (q_x, q_z)$ the momentum transfer along the surface and

$$\Lambda^{\alpha\beta}(E, \mathbf{q}_{\parallel}) = \int \frac{d^2 k_{\parallel}}{(2\pi)^2} \sum_{n=1}^{n_0} \text{Tr}_\sigma [S^\alpha \delta G_{nn}^\beta(E, \mathbf{k}_{\parallel}, \mathbf{q}_{\parallel})]_{11}. \quad (7)$$

In Eq. (7) the subscript ‘‘11’’ represents indices in Nambu particle-hole space, Tr_σ is the trace in spin space, and δG_{nn}^β denotes the change in the BdG Green’s function $G_{nn}^{(0)}$ due to scattering processes. For weak impurity potentials $V_{\mathbf{q}}^\beta$, disorder scattering can be treated within the Born approximation which yields

$$\delta G_{nn}^\beta(E, \mathbf{k}_{\parallel}, \mathbf{q}_{\parallel}) = \sum_{n'n''} G_{nn'}^{(0)}(E, \mathbf{k}'_{\parallel}) V_{n'n''}^\beta G_{n''n}^{(0)}(E, \mathbf{k}_{\parallel}), \quad (8)$$

with $\mathbf{k}'_{\parallel} = \mathbf{k}_{\parallel} + \mathbf{q}_{\parallel}$. The Fourier-transformed disorder potential

$$V_{n'n''}^\beta = \frac{1}{2\pi} \int dq_y e^{iq_y(n-n'')} V_{\mathbf{q}}^\beta = v_0 S^\beta \sum_{n''=1}^{n_0} \delta_{n,n''} \delta_{n',n''} \quad (9)$$

describes onsite impurities with strength $v_0 = 0.2$, which are assumed to be equally distributed among the $n_0 = 10$ outermost layers of the superconductor.

In closing this section, we remark that all the components of the response tensor $\delta\rho_s^{\alpha\beta}(E, \mathbf{q}_{\parallel})$, see Eq. (6), can, in principle, be measured using spin-polarized scanning tunneling spectroscopy. That is, the α -spin conductance channel can be selected via the polarization direction of the spin-polarized tunneling tip, whereas the component β of the spin scattering channel is determined by the direction of the external magnetic field.

A. QPI on the surface of centrosymmetric superconductors

Before discussing numerical simulations of QPI patterns on the surface of *noncentrosymmetric* superconductors, it is instructive to first consider *centrosymmetric* topological systems, whose quasiparticle surface states can be described by simple Dirac-type Hamiltonians. That is, we first study the FT-STs response of helical Majorana modes and arc states on the (010) surface of centrosymmetric superconductors. Effective Dirac-type Hamiltonians encoding the low-energy physics of these surface states are derived in Appendix A. Due to the simplicity of these surface Hamiltonians, it is possible to derive analytical expressions for the QPI patterns.

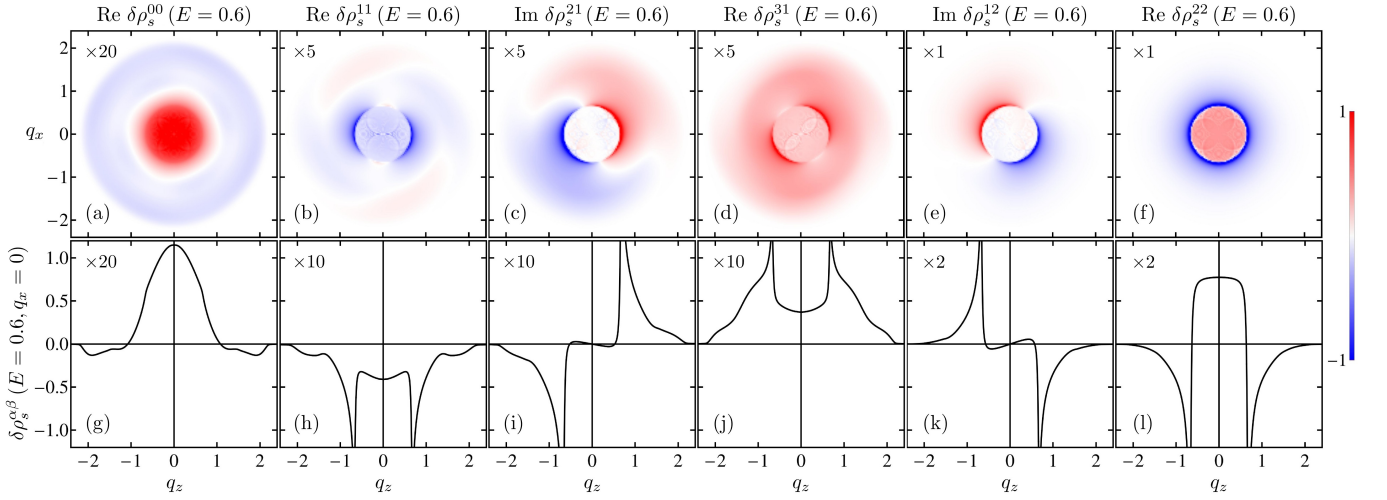


FIG. 2. (Color online) Ordinary and spin-resolved FT-STs interference patterns $\delta\rho_s^{\alpha\beta}(E, \mathbf{q}_{\parallel})$ arising from magnetic and nonmagnetic scattering processes on the surface of a fully gapped topological superconductor with cubic point group O . The top row shows density plots of $\delta\rho_s^{\alpha\beta}(E = 0.6, \mathbf{q}_{\parallel})$ as a function of momentum transfer $\mathbf{q}_{\parallel} = (q_x, q_z)$. The bottom row gives the corresponding cuts along the $q_x = 0$ line. Here we set $\lambda = -2.0$ and $\Delta_s = 0.5$. The color scale for the density plots in panels (a)-(d) and the vertical scale in panels (g)-(l) have been multiplied by a factor as indicated for clarity.

1. Helical Majorana modes

The universal properties of helical Majorana surface states in superconductors with inversion symmetry are described by the massless Dirac Hamiltonian [cf. Eqs. (A9) and (A10)]

$$H_{\text{MS}}(\mathbf{k}_{\parallel}) = \Delta_t(k_z\sigma_1 - k_x\sigma_3) + v_0\sigma_2, \quad (10)$$

where $v_0\sigma_2$ is an onsite disorder potential describing impurity spins polarized along the y axis. Remarkably, as shown in Appendix A, nonmagnetic impurity scattering on the surface of centrosymmetric topological superconductors is forbidden by symmetry, while magnetic impurities only couple via their out-of-plane spin component to the surface states. As mentioned in Sec. II B, the helical Majorana mode is spin polarized, with the spin direction locked to the momentum direction. For the surface state (10), we find that spin and momentum directions are inclined at a right angle to each other. This is in contrast to helical Majorana states of *noncentrosymmetric* superconductors, where spin and momentum are in general locked to each other at an angle different from $\pm\pi/2$, see Fig. 1(a) and discussion in Sec. III B.

The QPI patterns of the Majorana state (10) is obtained from Eq. (6) upon replacing $\Lambda^{\alpha\beta}(E, \mathbf{q}_{\parallel})$ by

$$\Lambda_{\text{MS}}^{\alpha\beta=2}(E, \mathbf{q}_{\parallel}) = \frac{v_0}{2} \int \frac{d^2k_{\parallel}}{(2\pi)^2} \text{Tr} \left[\sigma_{\alpha} G_{\text{MS}}^{(0)}(i\varpi, \mathbf{k}'_{\parallel}) \sigma_2 G_{\text{MS}}^{(0)}(i\varpi, \mathbf{k}_{\parallel}) \right]_{i\varpi \rightarrow E+i\eta}, \quad (11)$$

where $\mathbf{k}'_{\parallel} = \mathbf{k}_{\parallel} + \mathbf{q}_{\parallel}$, ϖ denotes the Matsubara frequency, and $G_{\text{MS}}^{(0)}(i\varpi, \mathbf{k}_{\parallel}) = [i\varpi - \Delta_t(k_z\sigma_1 - k_x\sigma_3)]^{-1}$ is the bare Green's function of the helical Majorana mode. In deriving Eq. (11) we have made use of Eq. (A11) from Appendix A 1. Note that since the surface state (10) only couples to y -polarized impurity spins, the FT-STs signal $\delta\rho_s^{\alpha\beta}$ vanishes for

$\beta \neq 2$. Inserting the definition of the Green's function $G_{\text{MS}}^{(0)}$ into Eq. (11) we obtain the integral

$$\Lambda_{\text{MS}}^{\alpha 2} = \int \frac{d^2k_{\parallel}}{(2\pi)^2} \frac{(-v_0)L_{\text{MS}}^{\alpha}}{[\varpi^2 + \Delta_t^2 k_{\parallel}^2][\varpi^2 + \Delta_t^2 (\mathbf{k}_{\parallel} + \mathbf{q}_{\parallel})^2]}, \quad (12)$$

where the numerator is given by $L_{\text{MS}}^{\alpha} = (0, \Delta_t\varpi q_x, \Delta_t^2 \mathbf{k}_{\parallel} \cdot \mathbf{k}'_{\parallel} + \varpi^2, \Delta_t\varpi q_z)$. The explicit solution to this integral can be found using the Feynman parametrization,⁴⁰

$$\Lambda_{\text{MS}}^{\alpha 2}(i\varpi, \mathbf{q}_{\parallel}) = \begin{cases} \frac{v_0}{2\pi\Delta_t^2} \frac{q_x}{|\mathbf{q}_{\parallel}|} \zeta \mathcal{F}(\zeta) & \text{if } \alpha = 1 \\ -\frac{v_0}{2\pi\Delta_t^2} \left[\frac{1}{2} \ln \left(1 + \frac{\Omega^2}{\varpi^2} \right) + \mathcal{F}(\zeta) \right] & \text{if } \alpha = 2 \\ \frac{v_0}{2\pi\Delta_t^2} \frac{q_x}{|\mathbf{q}_{\parallel}|} \zeta \mathcal{F}(\zeta) & \text{if } \alpha = 3, \end{cases} \quad (13)$$

and $\Lambda_{\text{MS}}^{\alpha\beta} = 0$ otherwise. Equation (13) is expressed in terms of the function

$$\mathcal{F}(\zeta) = \frac{1}{\sqrt{-\zeta^2 - 1}} \arctan \frac{1}{\sqrt{-\zeta^2 - 1}}, \quad (14)$$

with the dimensionless variable $\zeta = 2\varpi / (\Delta_t |\mathbf{q}_{\parallel}|)$ and Ω is a momentum cutoff that sets the range of validity for the Dirac-type Hamiltonian (10).

Interestingly, we find that the ordinary FT-STs signal $\delta\rho_s^{0\beta}$ in the presence of weak magnetic impurities vanishes identically. This is a consequence of time-reversal symmetry, as shown in Appendix B. The spin-resolved FT-STs response $\delta\rho_s^{\alpha 2}$, with $\alpha \in \{1, 2, 3\}$, on the other hand, is nonzero and exhibits an inverse square-root singularity at the momenta $|\mathbf{q}_{\parallel,0}| = 2E/\Delta_t$ (cf. Fig. 2). This singularity arises due to

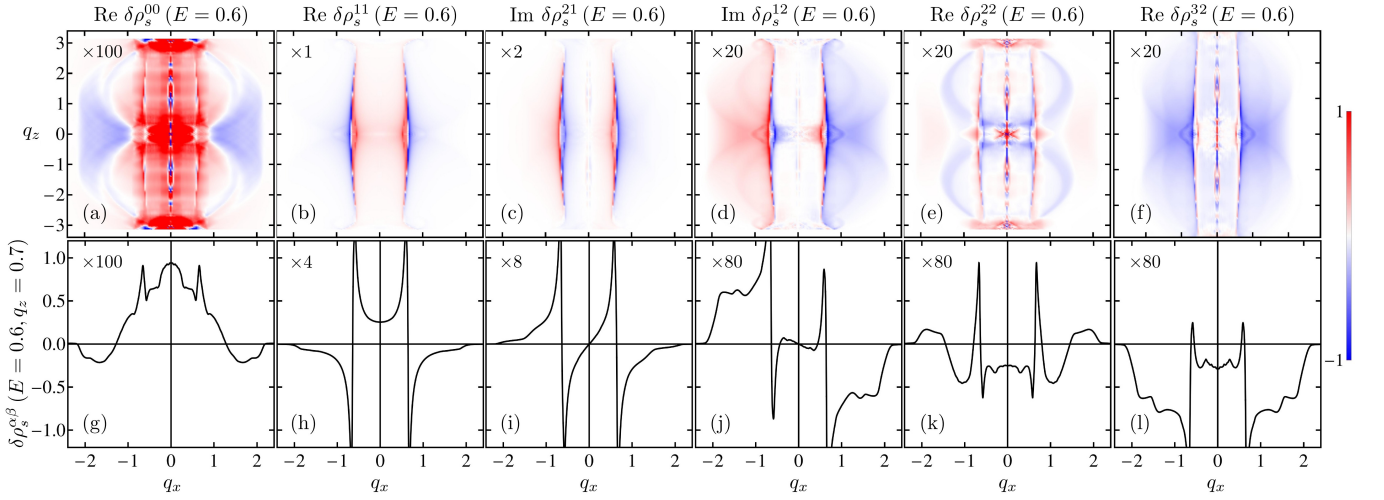


FIG. 3. (Color online) Ordinary and spin-resolved FT-STs response $\delta\rho_s^{\alpha\beta}(E, \mathbf{q}_{\parallel})$ for a nodal NCS with tetragonal point group C_{4v} , $\lambda = -2.0$, and $\Delta_s = 0.5$. Top and bottom rows show density plots and cuts along the $q_z = 0.7$ line, respectively. The color scale for the density plots in (a)–(f) and the vertical scale in (g)–(l) have been multiplied by a factor as indicated for clarity.

backscattering processes between states at momenta $+\mathbf{q}_{\parallel,0}/2$ and $-\mathbf{q}_{\parallel,0}/2$. Furthermore, $\delta\rho_s^{12}$ and $\delta\rho_s^{32}$ have an interesting angular dependence on the momentum transfer \mathbf{q}_{\parallel} with a twofold symmetry and nodes along the q_z and q_x axes, respectively. In contrast, $\delta\rho_s^{22}$ is circularly symmetric in \mathbf{q}_{\parallel} .

2. Arc surface states

At probe energies $E \ll \Delta_t$, the universal physics of the arc surface states of centrosymmetric superconductors can be captured by the effective low-energy Hamiltonian

$$H_{AS}(\mathbf{k}_{\parallel}) = -\Delta_t k_x \sigma_3 - v_0 \sigma_1, \quad (15)$$

where the surface momentum $\mathbf{k}_{\parallel} = (k_x, k_z)$ is restricted to the range $|k_z| < k_z^0$ and k_z^0 is half the length of the arc state in the surface Brillouin zone. In Eq. (15) the onsite potential $v_0 \sigma_1$ describes impurity spins polarized along the x axis. Interestingly, all other scattering channels are absent due to symmetry constraints. A detailed derivation of Hamiltonian (15) is presented in Appendix A 2. We observe that the surface state (15) is fully polarized along the z spin axis, in contrast to arc states in noncentrosymmetric superconductors, which in general show finite spin polarizations both along the y and z directions, see Fig. 1(b).

Let us now compute the FT-STs response function for the arc state (15). Combining Eq. (15) with Eq. (A20) we find that the QPI signal is given by Eq. (6) with $\Lambda^{\alpha\beta}(E, \mathbf{q}_{\parallel})$ replaced by

$$\Lambda_{AS}^{\alpha\beta=1}(E, \mathbf{q}_{\parallel}) = -\frac{v_0}{2} (-1)^\alpha \int \frac{dk_{\parallel}}{(2\pi)^2} \quad (16)$$

$$\times \text{Tr} \left[\sigma_\alpha G_{AS}^{(0)}(i\varpi, \mathbf{k}'_{\parallel}) \sigma_1 G_{AS}^{(0)}(i\varpi, \mathbf{k}_{\parallel}) \right]_{i\varpi \rightarrow E+i\eta},$$

where $G_{AS}^{(0)}(i\varpi, \mathbf{k}_{\parallel}) = \Theta(k_z^0 - |k_z|) [i\varpi + \Delta_t k_x \sigma_3]^{-1}$ is the Green's function of the unperturbed system, Θ denotes the

unit step function, and $\mathbf{k}'_{\parallel} = \mathbf{k}_{\parallel} + \mathbf{q}_{\parallel}$. Because the arc state (15) only interacts with x -polarized magnetic impurities, the QPI pattern $\delta\rho_s^{\alpha\beta}$ is identically zero for $\beta \neq 1$. We now evaluate the above integral by first inserting the bare Green's functions and then performing the k_z integration. This gives

$$\Lambda_{AS}^{\alpha 1} = \int \frac{dk_x}{(2\pi)^2} \frac{v_0 (|q_z| - 2k_z^0) \Theta(2k_z^0 - |q_z|) L_{AS}^\alpha}{[\varpi^2 + \Delta_t^2 k_x^2] [\varpi^2 + \Delta_t^2 (k_x + q_x)^2]}, \quad (17)$$

where we have introduced the shorthand notation $L_{AS}^\alpha = (0, \Delta_t^2 k_x (k_x + q_x) + \varpi^2, \Delta_t \varpi q_x, 0)$. This integral can be computed explicitly to

$$\Lambda_{AS}^{\alpha 1}(i\varpi, \mathbf{q}_{\parallel}) = \begin{cases} \frac{v_0 \varpi (|q_z| - 2k_z^0) \Theta(2k_z^0 - |q_z|)}{\pi \Delta_t (4\varpi^2 + \Delta_t^2 q_x^2)} & \text{if } \alpha = 1 \\ \frac{v_0 q_x (|q_z| - 2k_z^0) \Theta(2k_z^0 - |q_z|)}{2\pi (4\varpi^2 + \Delta_t^2 q_x^2)} & \text{if } \alpha = 2, \end{cases} \quad (18)$$

and zero otherwise.

As before, we find that due to time-reversal invariance the non-spin-resolved QPI patterns resulting from weak magnetic impurities are vanishing. The spin-polarized FT-STs signals, however, are finite and show an interesting dependence on momentum transfer \mathbf{q}_{\parallel} (cf. Fig. 3). For $\alpha \in \{1, 2\}$, $\delta\rho_s^{\alpha 1}$ exhibits a $1/q_x$ divergence at $|q_{x,0}| = 2E/\Delta_t$. This singularity is due to backscattering processes among states with x momentum component $+q_{x,0}/2$ and $-q_{x,0}/2$. In addition, we find that $\delta\rho_s^{11}$ is an even function of q_x , whereas $\delta\rho_s^{21}$ is odd in q_x .

B. Numerical simulations of QPI patterns on the surface of noncentrosymmetric superconductors

In this section, we study the FT-STs response of helical Majorana modes, arc states, and zero-energy flat bands on the surface of *noncentrosymmetric* superconductors. That is,

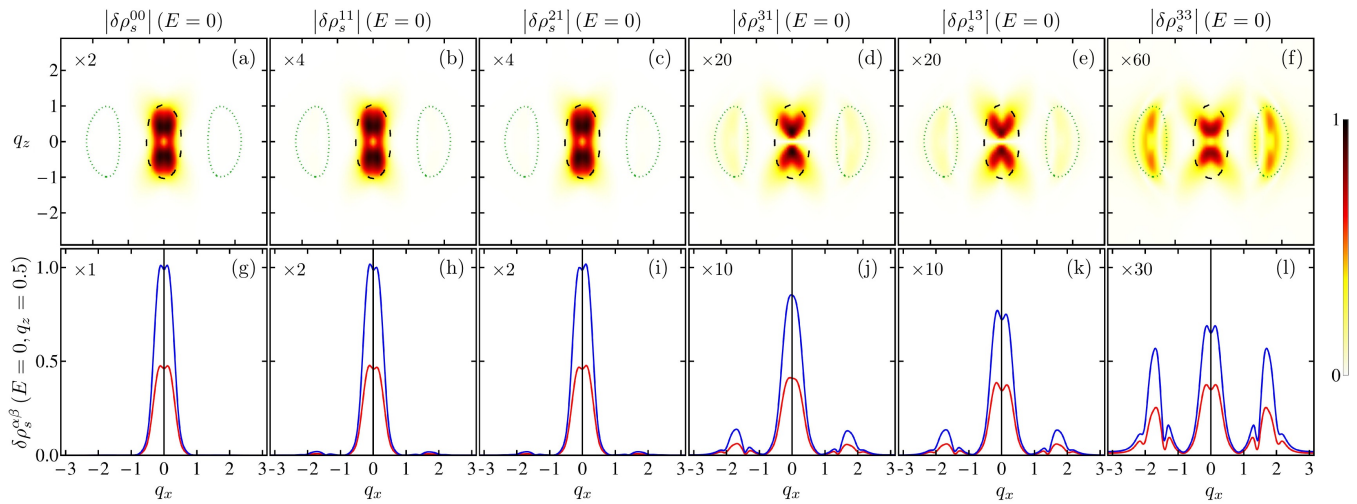


FIG. 4. (Color online) Amplitude of the ordinary and spin-resolved FT-STs signal $\delta\rho_s^{\alpha\beta}(E, \mathbf{q}_{\parallel})$ for a nodal NCS with flat-band surface states. Here, the SOC vector $\mathbf{l}_{\mathbf{k}}$ is given by Eq. (2c), $\lambda = -0.5$, and $\Delta_s = 4.0$. The top row shows density plots of $\delta\rho_s^{\alpha\beta}(E = 0, \mathbf{q}_{\parallel})$ as a function of \mathbf{q}_{\parallel} for an intrinsic broadening $\eta = 0.005$. Green dotted and black dashed lines indicate the boundary of the regions corresponding to inter- and intraband scattering, respectively. Panels (g)–(l) display cuts of $\delta\rho_s^{\alpha\beta}(E = 0, \mathbf{q}_{\parallel})$ along the line $q_z = 0$ for $\eta = 0.005$ (red) and $\eta = 0.0025$ (blue). The color scale for the density plots in (b)–(f) and the vertical scale in (h)–(l) have been multiplied by a factor as indicated for clarity.

we consider the QPI patterns on the surface of an unconventional superconductor described by Hamiltonian (1) with finite SOC strength λ and nonzero spin-triplet and spin-singlet pairing components. Unfortunately, for noncentrosymmetric systems, it is no longer possible to derive the FT-STs signal analytically. Therefore we resort to numerical simulations and compute the QPI patterns through exact diagonalization of the BdG Hamiltonian (1) in a slab geometry with surfaces perpendicular to the (010) direction.

1. Helical Majorana modes

In Fig. 2 is shown the FT-STs response $\delta\rho_s^{\alpha\beta}$ of a helical Majorana mode on the surface of an O point-group NCS to nonmagnetic ($\beta = 0$) and magnetic impurities ($\beta \in \{1, 2, 3\}$). As opposed to centrosymmetric superconductors, we find that Majorana modes of NCSs couple to both nonmagnetic and magnetic scatterers with arbitrary spin polarization (cf. Sec. III A 1). Hence, as shown in Appendix B, $\delta\rho_s^{00}$ and $\delta\rho_s^{\alpha\beta}$ with $\alpha, \beta \in \{1, 2, 3\}$ are in general nonzero, whereas $\delta\rho_s^{0\beta}$ and $\delta\rho_s^{\alpha 0}$ with $\alpha, \beta \in \{1, 2, 3\}$ are, due to time-reversal invariance, vanishing within the Born approximation. Furthermore, we find that four pairs of elements of the FT-STs response tensor are related to each other by crystallographic point-group symmetries (Appendix B). Thus, we plot in Fig. 2 only the six independent nonzero elements of $\delta\rho_s^{\alpha\beta}$, which are either purely real or purely imaginary.

Interestingly, nonmagnetic impurities give rise to only weak, nonsingular FT-STs response, see Figs. 2(a) and 2(g). This is due to the absence of elastic backscattering processes between states at momenta $+\mathbf{q}_{\parallel,0}/2$ and $-\mathbf{q}_{\parallel,0}/2$, where

$|\mathbf{q}_{\parallel,0}| = 2E/\Delta_t$. These nonmagnetic backscattering processes are prohibited by time-reversal symmetry, due to the opposite spin polarizations of states at opposite momenta. As a result, $\delta\rho_s^{00}$ only exhibits a kink at $|\mathbf{q}_{\parallel,0}|$, but no singularity. In the presence of magnetic impurities, however, spin-flip scattering processes are allowed. This leads to an inverse square-root singularity in $\delta\rho_s^{\alpha\beta}$ at $|\mathbf{q}_{\parallel,0}| = 2E/\Delta_t$, see Figs. 2(h)–(l).

In passing, we point out some interesting features in the angular dependence of $\delta\rho_s^{\alpha\beta}$ on transfer momentum \mathbf{q}_{\parallel} . As in the centrosymmetric case, the dependence of $\delta\rho_s^{\alpha\beta}$ on \mathbf{q}_{\parallel} in Figs. 2(b)–(e) exhibits a π rotational symmetry about the origin, i.e., $\delta\rho_s^{\alpha\beta}(\mathbf{q}_{\parallel}) = [\delta\rho_s^{\alpha\beta}(-\mathbf{q}_{\parallel})]^*$. Twofold symmetries with high-symmetry lines along the vertical or horizontal axes, however, are absent. We observe that the different angular dependence between the centrosymmetric and noncentrosymmetric cases is due to differences in the spin polarization [see Fig. 1(d)]. While in the centrosymmetric case, spin and momentum of the Majorana mode (13) are locked to each other at a right angle, in NCSs the angle between spin and momentum directions of the Majorana surface states differs from $\pm\pi/2$ and, moreover, varies strongly as a function of distance from the surface layer. This dependence of the spin polarization on layer index n results in the absence of any twofold mirror symmetries in the QPI patterns of Figs. 2(b)–(e).

2. Arc surface states

The FT-STs response of an arc state on the surface of a C_{4v} point-group NCS is shown in Fig. 3. In order to discuss energy and momentum dependence of these QPI patterns, we first

point out that the arc surface state can essentially be viewed as a quasi-one-dimensional analog of the two-dimensional Majorana mode of the previous subsection. In other words, a description of the arc state can be obtained from the O point-group NCS by interchanging x and y components of the spin operator and by setting $k_z = 0$, see Eqs. (2a) and (2b). This explains the similarities in the QPI patterns of Fig. 3 with the response at $q_z = 0$ shown in Fig. 2.

As in Figs. 2(a) and 2(g), we find that the FT-STs signal produced by nonmagnetic impurities is weak and non-singular, since spin-flip backscattering is prohibited by time-reversal symmetry. Hence $\delta\rho_s^{00}$ in Figs. 3(a) and 3(g) only shows a nondivergent kink- or peaklike feature at $|q_{x,0}| = 2E/\Delta_t$. Magnetic impurities, on the other hand, give rise to a strong and divergent response in the spin-resolved FT-STs [see Figs. 3(b)–(f) and 3(h)–(l)]. Similar to Eq. (18), there is a divergence in $\delta\rho_s^{\alpha\beta}$ at $|q_{x,0}| = 2E/\Delta_t$. We note that due to the different dimensionality of the momentum phase space, this is not an inverse square-root singularity as in Figs. 2(h)–(l), but shows a $1/q_x$ dependence.

3. Zero-energy flat bands

Finally, we discuss the FT-STs response of zero-energy flat bands on the surface of a C_2 point-group NCS, which is shown in Fig. 4. As before, we find that due to time-reversal symmetry the only nonzero elements of the response tensor $\delta\rho_s$ are $\delta\rho_s^{00}$ and $\delta\rho_s^{\alpha\beta}$ with $\alpha, \beta \in \{1, 2, 3\}$. Since lattice point-group symmetries relate four pairs of entries of $\delta\rho_s$ to each other (see Appendix B), we plot in Fig. 4 only the six independent nonzero elements of $\delta\rho_s^{\alpha\beta}$.

The C_2 point-group NCS as defined by Eqs. (1) and (2c) exhibits two different zero-energy flat bands on the (010) surface, one with negative surface momentum $k_x < 0$ and one with positive momentum $k_x > 0$, see Figs. 1(c) and 1(f). Hence, in the presence of impurities, it is useful to distinguish between interband scattering with transfer momentum $|q_x| \lesssim 1.0$ and intraband scattering with $|q_x| \gtrsim 1.0$, as indicated in Figs. 4(g)–(l) by the green dotted and black dashed ellipses, respectively.

Due to the opposite spin polarizations of the two zero-energy flat bands, time-reversal-preserving interband scattering is considerably suppressed.²⁰ Hence the part of the ordinary FT-STs signal $\delta\rho_s^{00}$ that corresponds to interband scattering [green dotted ellipses in Fig. 4(a)] is very weak, whereas the one corresponding to intraband scattering [black dashed ellipses in Fig. 4(a)] is strong and divergent. Magnetic impurities, on the other hand, give rise to both strong inter- and intraband backscattering. Consequently, the FT-STs response shown in Figs. 4(b)–(f) and 4(h)–(l) exhibits strong divergences both for large and small transfer momenta, i.e., within the regions in Figs. 4(b)–(f) bounded by green dotted and black dashed lines, respectively.

IV. SUMMARY AND DISCUSSION

In summary, we have determined the universal features in the QPI patterns produced by magnetic and nonmagnetic impurities on the surface of time-reversal invariant topological superconductors. An explicit analytical expression was found for the energy and momentum dependence of the QPI patterns on the surface of centrosymmetric topological superconductors. For noncentrosymmetric systems, on the other hand, we have numerically determined the ordinary and spin-resolved FT-STs response.

We have studied both fully gapped and nodal topological superconductors and considered three different types of surface states: helical Majorana modes, arc surface states, and zero-energy flat bands. Due to SOC, these surface states exhibit an intricate helical spin texture, where the spin polarization strongly depends on the surface momentum. Time-reversal invariance ensures that surface states with opposite momenta have opposite spin polarizations, which leads to the absence of backscattering from nonmagnetic impurities. As a consequence, the ordinary FT-STs signal of Majorana modes and arc surface states due to nonmagnetic scattering is weak and nondivergent. In the case of the flat-band surface states, the absence of backscattering results in a suppression of the QPI signal produced by scattering processes with large momentum transfer. In the presence of magnetic impurities, however, spin-flip scattering is possible, and hence backscattering leads to a large and divergent FT-STs response for all three types of surface states.

Our results highlight the unique power of the FT-STs technique to detect topological surface states in unconventional superconductors. We have demonstrated that the FT-STs response allows to clearly distinguish among the three different types of surface states that generically occur in time-reversal invariant topological superconductors. Moreover, the analysis of QPI patterns can be used to infer information about the pairing symmetry and the topological characteristics of the superconducting state.

ACKNOWLEDGMENTS

The authors thank F. Assaad, P. Brydon, C. Timm, P. Wahl, and A. Yazdani for useful discussions.

Appendix A: Low-energy models for the surface states of centrosymmetric superconductors

In this appendix, we derive low-energy effective Hamiltonians describing the surface states of *centrosymmetric* topological superconductors with time-reversal symmetry. To that end, we consider Hamiltonian (1) with vanishing SOC strength λ , zero singlet pairing component Δ_s , and surface perpendicular to the y axis. The surface plane is chosen to be at $y = 0$, where the bulk superconductor and the vacuum occupy the half-spaces $y > 0$ and $y < 0$, respectively. The derivation of

the surface states of topological centrosymmetric superconductors proceeds along similar lines as for the case of topological insulators.^{38,39}

1. Helical Majorana modes

First, we examine helical Majorana modes that appear at the surface of fully gapped topological superconductors. For concreteness, we consider a centrosymmetric system with cubic crystallographic point group O , i.e., Hamiltonian (1) with $\lambda = 0$, $\Delta_s = 0$, and \mathbf{d} -vector $\mathbf{d}_{\mathbf{k}}$ given by Eq. (2a). Focusing on low energies, we perform a small-momentum expansion near the Γ point. This yields

$$\tilde{H}(\mathbf{k}) = \begin{pmatrix} \tilde{\varepsilon}_{\mathbf{k}}\sigma_0 & i\Delta_t(\mathbf{k} \cdot \boldsymbol{\sigma})\sigma_2 \\ -i\Delta_t\sigma_2(\mathbf{k} \cdot \boldsymbol{\sigma}) & -\tilde{\varepsilon}_{\mathbf{k}}\sigma_0 \end{pmatrix}, \quad (\text{A1})$$

where $\tilde{\varepsilon}_{\mathbf{k}} = 3t - \mu - \frac{t}{2}(k^2 + k_y^2)$ and $k^2 = k_x^2 + k_z^2$. With the trial wavefunction $\psi(y) = \psi_{\kappa} e^{\kappa y}$, which is localized at the surface $y = 0$, we obtain the eigenvalue equation

$$\tilde{H}(k, -i\partial_y)\psi(y) = E\psi(y), \quad (\text{A2})$$

where we have replaced k_y by $-i\partial_y$. Solving the secular equation, $\det[\tilde{H}(k_x, -i\kappa, k_z) - E\mathbb{1}] = 0$, gives four solutions for $\kappa(E)$ denoted as $\beta\kappa_{\alpha}(E)$, with $\alpha \in \{1, 2\}$, $\beta \in \{+, -\}$, and

$$\kappa_{\alpha}(E) = \frac{1}{t} [2\Delta_t^2 - 2L + k^2 t^2 + (-1)^{\alpha} 2R]^{\frac{1}{2}}, \quad (\text{A3})$$

where we have introduced the shorthand notation $L = (3t - \mu)t$ and $R = \sqrt{\Delta_t^4 - 2\Delta_t^2 L + E^2 t^2}$. For each of the four roots $\kappa_{\alpha}(E)$, the kernel of the secular equation is spanned by two independent basis vectors, given by

$$\psi_{\alpha\beta 1} = \begin{pmatrix} \Delta_t t k_z \\ \Delta_t t (\beta\kappa_{\alpha} + k_x) \\ 0 \\ Et - L + \frac{t^2}{2}(k^2 - \kappa_{\alpha}^2) \end{pmatrix}, \quad (\text{A4a})$$

$$\psi_{\alpha\beta 2} = \begin{pmatrix} \Delta_t t (\beta\kappa_{\alpha} - k_x) \\ \Delta_t t k_z \\ Et - L + \frac{t^2}{2}(k^2 - \kappa_{\alpha}^2) \\ 0 \end{pmatrix}. \quad (\text{A4b})$$

With this, we obtain the following ansatz for the surface state wave function

$$\Psi(\mathbf{k}_{\parallel}, y) = \sum_{\alpha, \gamma \in \{1, 2\}} \sum_{\beta = \pm} C_{\alpha\beta\gamma} \psi_{\alpha\beta\gamma} e^{\beta\kappa_{\alpha} y}, \quad (\text{A5})$$

where $\mathbf{k}_{\parallel} = (k_x, k_z)$ and the coefficients $C_{\alpha\beta\gamma}$ are determined by the boundary conditions $\Psi(\mathbf{k}_{\parallel}, y = 0) = 0$ and $\Psi(\mathbf{k}_{\parallel}, y \rightarrow +\infty) = 0$. The secular equation for the coefficients $C_{\alpha\beta\gamma}$ leads to the condition

$$2L = (k^2 + \kappa_1 \kappa_2) t^2, \quad (\text{A6})$$

which together with Eq. (A3) yields the dispersion for the surface states

$$E_{\pm}(\mathbf{k}_{\parallel}) = \pm \Delta_t k. \quad (\text{A7})$$

The surface state wave functions at the Γ point are found to be

$$\Psi_{\text{MS}}^{\pm}(\mathbf{k}_{\parallel} = 0, y) = \varphi_{\text{MS}}^{\pm} [e^{-\kappa_1(0)y} - e^{-\kappa_2(0)y}], \quad (\text{A8a})$$

$$\varphi_{\text{MS}}^+ = \frac{1}{\sqrt{2}} \begin{pmatrix} 1 \\ 0 \\ 1 \\ 0 \end{pmatrix}, \quad \varphi_{\text{MS}}^- = \frac{1}{\sqrt{2}} \begin{pmatrix} 0 \\ 1 \\ 0 \\ 1 \end{pmatrix}, \quad (\text{A8b})$$

where $\kappa_{\alpha}(0)$ is defined in Eq. (A3). From condition (A6) it follows that zero-energy surface states can exist if $\kappa_1(0)$ and $\kappa_2(0)$ are either both real or complex conjugate partners. In the former case, i.e., when $\Delta_t^2 > 2L > 0$, the wave functions decay monotonically into the bulk with the decay lengths $\kappa_{\alpha}^{-1}(0)$. For $\Delta_t^2 < 2L$, on the other hand, $\kappa_{\alpha}(0)$ are complex, which leads to an oscillatory decay of the wave functions with inverse decay length $\text{Re}[\kappa_{\alpha}(0)] = \Delta_t/t$ and oscillation frequencies $\text{Im}[\kappa_{\alpha}(0)]$.

An effective low-energy Hamiltonian for the surface states $\Psi_{\text{MS}}^{\pm}(\mathbf{k}_{\parallel})$ can be derived by projecting $\tilde{H}(\mathbf{k})$, see Eq. (A1), onto the subspace $\Psi_{\text{MS}} = \{\varphi_{\text{MS}}^+, \varphi_{\text{MS}}^-\}$ formed by the two surface-state wave functions (A8). This yields an effective 2×2 Hamiltonian:

$$\langle \Psi_{\text{MS}} | \tilde{H}(\mathbf{k}) | \Psi_{\text{MS}} \rangle = \Delta_t (k_z \sigma_1 - k_x \sigma_3), \quad (\text{A9})$$

which has the same dispersion as Eq. (A7). In order to compute the ordinary and spin-resolved FT-STs for the helical Majorana states described by Eq. (A9), we need to project the impurity potential $V_{\mathbf{q}}^{\beta}$, Eq. (5), onto the surface-state subspace Ψ_{MS} . Using Eq. (4), we find

$$\langle \Psi_{\text{MS}} | V_{\mathbf{q}}^{\beta} | \Psi_{\text{MS}} \rangle = \begin{cases} v_{\mathbf{q}} \sigma_2 & \text{if } \beta = 2 \\ 0 & \text{otherwise.} \end{cases} \quad (\text{A10})$$

Remarkably, it follows that nonmagnetic scattering is absent, whereas for magnetic impurities only the out-of-plane spin component couples to the surface states. Finally, to evaluate the FT-STs response, Eq. (3), we also need to determine the electronlike parts of the charge and spin operators (4) within the surface-state subspace. We have

$$\langle \Psi_{\text{MS}} | P_e S^{\alpha} | \Psi_{\text{MS}} \rangle = \frac{1}{2} \sigma_{\alpha}, \quad (\text{A11})$$

where $P_e = \frac{1}{2} (\mathbb{1} + \sigma_3 \otimes \sigma_0)$.

2. Arc surface states

Second, we study arc surface states that exist, for example, at the surface of centrosymmetric superconductors with point nodes in the BdG excitation spectrum. For concreteness, we consider a system with a \mathbf{d} -vector $\mathbf{d}_{\mathbf{k}}$ given by Eq. (2b). Furthermore, neglecting the effects of noncentrosymmetry, we set the SOC strength λ and the spin-singlet component Δ_s of the superconducting gap to zero. Within a small-momentum expansion near $k_x = k_y = 0$, the superconductor is described by

$$\tilde{H}(\mathbf{k}) = \begin{pmatrix} \tilde{\varepsilon}_{\mathbf{k}}\sigma_0 & -\Delta_t(k_y\sigma_3 + ik_x\sigma_0) \\ -\Delta_t(k_y\sigma_3 - ik_x\sigma_0) & -\tilde{\varepsilon}_{\mathbf{k}}\sigma_0 \end{pmatrix},$$

$$(A12)$$

where $\tilde{\varepsilon}_{\mathbf{k}} = 2t + t \cos k_z - \mu - \frac{t}{2}(k_x^2 + k_y^2)$. As before, the ansatz for the surface-bound-state wave function is taken to be $\Psi(y) = \Psi_{\kappa} e^{\kappa y}$, with the inverse decay length κ . From the secular equation, we obtain four solutions for $\kappa(E)$ given by $\pm \kappa_{\alpha}(E)$:

$$\kappa_{\alpha}(E) = \frac{1}{t} [2\Delta_t^2 - 2L + k_x^2 t^2 + (-1)^{\alpha} 2R]^{\frac{1}{2}}, \quad (A13)$$

with $\alpha \in \{1, 2\}$, $R = \sqrt{\Delta_t^4 - 2\Delta_t^2 L + E^2 t^2}$, and $L = (2t + t \cos k_z - \mu)t$. Repeating similar steps as above, we obtain for the surface-state trial wave function

$$\Psi(\mathbf{k}_{\parallel}, y) = \sum_{\alpha, \gamma \in \{1, 2\}} \sum_{\beta = \pm} C_{\alpha\beta\gamma} \psi_{\alpha\beta\gamma} e^{\beta \kappa_{\alpha} y}, \quad (A14)$$

with $\mathbf{k}_{\parallel} = (k_x, k_z)$ and the two independent vectors

$$\psi_{\alpha\beta 1} = \begin{pmatrix} 0 \\ -i\Delta_t t (\beta \kappa_{\alpha} + k_x) \\ 0 \\ Et - L + \frac{t^2}{2} (k_x^2 - \kappa_{\alpha}^2) \end{pmatrix}, \quad (A15a)$$

$$\psi_{\alpha\beta 2} = \begin{pmatrix} +i\Delta_t t (\beta \kappa_{\alpha} - k_x) \\ 0 \\ Et - L + \frac{t^2}{2} (k_x^2 - \kappa_{\alpha}^2) \end{pmatrix}. \quad (A15b)$$

A surface state occurs if the coefficients $C_{\alpha\beta\gamma}$ can be chosen such that the wave function $\Psi(\mathbf{k}_{\parallel}, y)$ satisfies the boundary conditions $\Psi(\mathbf{k}_{\parallel}, y = 0) = 0$ and $\Psi(\mathbf{k}_{\parallel}, y \rightarrow +\infty) = 0$. After some algebra, this leads to the existence condition for the surface states:

$$2L = (k_x^2 + \kappa_1 \kappa_2) t^2. \quad (A16)$$

Combining Eqs. (A13) and (A16) gives the dispersion $E_{\pm}(\mathbf{k}_{\parallel}) = \pm \Delta_t k_x$. For the surface-state wave functions at $k_x = 0$, we find

$$\Psi_{\text{AS}}^{\pm}(k_x = 0, k_z, y) = \varphi_{\text{AS}}^{\pm} [e^{-\kappa_1(0)y} - e^{-\kappa_2(0)y}], \quad (A17a)$$

$$\varphi_{\text{AS}}^+ = \frac{1}{\sqrt{2}} \begin{pmatrix} -i \\ 0 \\ +1 \\ 0 \end{pmatrix}, \quad \varphi_{\text{AS}}^- = \frac{1}{\sqrt{2}} \begin{pmatrix} 0 \\ +i \\ 0 \\ +1 \end{pmatrix}, \quad (A17b)$$

where $\kappa_{\alpha}(0)$ is given by Eq. (A13). For $\Delta_t^2 > 2L > 0$, i.e., for $\arccos[(\Delta_t^2/(2t) - 2t + \mu)/t] < |k_z| < \arccos[(\mu - 2t)/t]$, the zero-energy wave functions (A17) decay exponentially and monotonically into the bulk, whereas for $2L > \Delta_t^2$ the exponential wave function decay is modulated by periodic oscillations with frequencies $\text{Im}[\kappa_{\alpha}(0)]$.

Projecting $\tilde{H}(\mathbf{k})$, see Eq. (A12), onto the subspace $\Psi_{\text{AS}} = \{\varphi_{\text{AS}}^-, \varphi_{\text{AS}}^+\}$ yields a low-energy effective Hamiltonian for the arc surface states:

$$\langle \Psi_{\text{AS}} | \tilde{H}(\mathbf{k}) | \Psi_{\text{AS}} \rangle = -\Delta_t k_x \sigma_3. \quad (A18)$$

The disorder potential $V_{\mathbf{q}}^{\beta}$, see Eq. (5), within the surface-state subspace Ψ_{AS} reads

$$\langle \Psi_{\text{AS}} | V_{\mathbf{q}}^{\beta} | \Psi_{\text{AS}} \rangle = \begin{cases} -v_{\mathbf{q}} \sigma_1 & \text{if } \beta = 1, \\ 0 & \text{otherwise,} \end{cases} \quad (A19)$$

whereas the projected electronlike parts of the charge and spin operators (4) are given by

$$\langle \Psi_{\text{AS}} | P_e S^{\alpha} | \Psi_{\text{AS}} \rangle = \frac{1}{2} (-1)^{\alpha} \sigma_{\alpha}, \quad (A20)$$

where $P_e = \frac{1}{2} (\mathbb{1} + \sigma_3 \otimes \sigma_0)$.

Appendix B: Symmetries of QPI patterns

1. Time-reversal symmetry

Time-reversal symmetry acts on the single-particle Green's function $G^{(0)}(\mathbf{k}_{\parallel}) = [E + i\eta - H(\mathbf{k}_{\parallel})]^{-1}$ as

$$U_T [G^{(0)}(-\mathbf{k}_{\parallel})]^T U_T^{\dagger} = G^{(0)}(\mathbf{k}_{\parallel}), \quad (B1)$$

where $U_T = \sigma_0 \otimes i\sigma_2$. Inserting relation (B1) into the definition of $\delta\rho_s$, see Eq. (6), yields

$$\delta\rho_s \left(U_T^{\dagger} [S^{\alpha}]^T U_T, U_T^{\dagger} [V^{\beta}]^T U_T; \mathbf{q}_{\parallel} \right) = \delta\rho_s(S^{\alpha}, V^{\beta}; \mathbf{q}_{\parallel}), \quad (B2)$$

where we have explicitly written out the dependence of $\delta\rho_s$ on the spin operations S^{α} and the impurity potential V^{β} . Since magnetic impurity potentials are odd under time-reversal symmetry, whereas S^0 is even, it follows that, within the Born approximation, $\delta\rho_s^{0\beta} = 0$, for $\beta \in \{1, 2, 3\}$. Similarly, we have $\delta\rho_s^{\alpha 0} = 0$, for $\alpha \in \{1, 2, 3\}$.

2. Point-group symmetries

As in the main text, we consider FT-STs patterns on a surface that is perpendicular to the y axis. Denoting those symmetry operations of the crystallographic point group that leave the (010) plane invariant by R , we find that $\delta\rho_s$ transforms under R as^{12,36}

$$\delta\rho_s \left(U_{\tilde{R}}^{\dagger} S^{\alpha} U_{\tilde{R}}, U_{\tilde{R}}^{\dagger} V^{\beta} U_{\tilde{R}}; R^{-1} \mathbf{q}_{\parallel} \right) = \delta\rho_s(S^{\alpha}, V^{\beta}; \mathbf{q}_{\parallel}), \quad (B3)$$

with $\tilde{R} = \det(R)R$, $U_{\tilde{R}} = \text{diag}(u_{\tilde{R}}, u_{\tilde{R}}^*)$, and $u_{\tilde{R}} = \exp[-i(\Theta/2)\hat{\mathbf{n}} \cdot \boldsymbol{\sigma}]$, where Θ is the angle of rotation of R and $\hat{\mathbf{n}}$ denotes the unit vector along the rotation axis.

a. Cubic point group O

For the cubic point-group O with $\mathbf{l}_{\mathbf{k}}$ given by Eq. (2a), Hamiltonian (1) is invariant under $\pi/2$ rotations about the y axis. Making use of Eq. (B3) with $R = R_{\hat{y}}$, where

$$R_{\hat{y}} = \begin{pmatrix} 0 & 0 & +1 \\ 0 & +1 & 0 \\ -1 & 0 & 0 \end{pmatrix}, \quad (B4)$$

yields

$$\delta\rho_s^{11}(\mathbf{q}_{\parallel}) = +\delta\rho_s^{33}(R_{\hat{y}}^{-1} \mathbf{q}_{\parallel}), \quad \delta\rho_s^{12}(\mathbf{q}_{\parallel}) = -\delta\rho_s^{32}(R_{\hat{y}}^{-1} \mathbf{q}_{\parallel}),$$

$$\delta\rho_s^{21}(\mathbf{q}_{\parallel}) = -\delta\rho_s^{23}(R_{\hat{y}}^{-1}\mathbf{q}_{\parallel}), \quad \delta\rho_s^{13}(\mathbf{q}_{\parallel}) = -\delta\rho_s^{31}(R_{\hat{y}}^{-1}\mathbf{q}_{\parallel}). \quad (\text{B5})$$

Furthermore, we find that the QPI patterns $\delta\rho_s^{00}(\mathbf{q}_{\parallel})$ and $\delta\rho_s^{22}(\mathbf{q}_{\parallel})$ are invariant under $\pi/2$ rotations, i.e., $\rho_s^{\alpha\alpha}(\mathbf{q}_{\parallel}) = \rho_s^{\alpha\alpha}(R_{\hat{y}}^{-1}\mathbf{q}_{\parallel})$, for $\alpha \in \{0, 2\}$.

b. Monoclinic point group C_2

In the case of the monoclinic point-group C_2 with \mathbf{l}_k given by Eq. (2c), we find that the (010) and (100) faces are equiv-

alent, i.e., the zero-energy states appearing on these two surfaces are identical. Hence we consider π rotations about the $\frac{1}{\sqrt{2}}(\hat{x} + \hat{y})$ axis with

$$R_{\hat{x}+\hat{y}} = \begin{pmatrix} 0 & +1 & 0 \\ +1 & 0 & 0 \\ 0 & 0 & -1 \end{pmatrix} \quad (\text{B6})$$

to obtain the following symmetry relations for $\delta\rho_s$:

$$\begin{aligned} \delta\rho_s^{11}(\mathbf{q}_{\parallel}) &= +\delta\rho_s^{22}(\tilde{\mathbf{q}}_{\parallel}), & \delta\rho_s^{12}(\mathbf{q}_{\parallel}) &= +\delta\rho_s^{21}(\tilde{\mathbf{q}}_{\parallel}), \\ \delta\rho_s^{13}(\mathbf{q}_{\parallel}) &= -\delta\rho_s^{23}(\tilde{\mathbf{q}}_{\parallel}), & \delta\rho_s^{31}(\mathbf{q}_{\parallel}) &= -\delta\rho_s^{32}(\tilde{\mathbf{q}}_{\parallel}), \end{aligned} \quad (\text{B7})$$

where $\tilde{\mathbf{q}}_{\parallel} = (q_x, -q_z)$.

-
- * a.schnyder@fkf.mpg.de
- ¹ E. Bauer and M. Sigrist, *Non-Centrosymmetric Superconductors: Introduction and Overview*, vol. 847 of *Lecture Notes in Physics* (Springer Berlin, 2012).
 - ² C. Iniotakis, N. Hayashi, Y. Sawa, T. Yokoyama, U. May, Y. Tanaka, and M. Sigrist, Phys. Rev. B **76**, 012501 (2007).
 - ³ M. Sato and S. Fujimoto, Phys. Rev. B **79**, 094504 (2009).
 - ⁴ A. P. Schnyder and S. Ryu, Phys. Rev. B **84**, 060504 (2011).
 - ⁵ A. P. Schnyder, S. Ryu, A. Furusaki, and A. W. W. Ludwig, Phys. Rev. B **78**, 195125 (2008).
 - ⁶ X.-L. Qi, T. L. Hughes, and S.-C. Zhang, Phys. Rev. B **81**, 134508 (2010).
 - ⁷ M. Sato and S. Fujimoto, Phys. Rev. Lett. **105**, 217001 (2010).
 - ⁸ P. M. R. Brydon, A. P. Schnyder, and C. Timm, Phys. Rev. B **84**, 020501 (2011).
 - ⁹ M. Sato, Y. Tanaka, K. Yada, and T. Yokoyama, Phys. Rev. B **83**, 224511 (2011).
 - ¹⁰ Y. Tanaka, Y. Mizuno, T. Yokoyama, K. Yada, and M. Sato, Phys. Rev. Lett. **105**, 097002 (2010).
 - ¹¹ K. Yada, M. Sato, Y. Tanaka, and T. Yokoyama, Phys. Rev. B **83**, 064505 (2011).
 - ¹² A. P. Schnyder, P. M. R. Brydon, and C. Timm, Phys. Rev. B **85**, 024522 (2012).
 - ¹³ Y. Tanaka, M. Sato, and N. Nagaosa, Journal of the Physical Society of Japan **81**, 011013 (2012).
 - ¹⁴ J. P. Dahlhaus, M. Gibertini, and C. W. J. Beenakker, Phys. Rev. B **86**, 174520 (2012).
 - ¹⁵ S. Matsuura, P.-Y. Chang, A. P. Schnyder, and S. Ryu, New Journal of Physics **15**, 065001 (2013).
 - ¹⁶ A. B. Vorontsov, I. Vekhter, and M. Eschrig, Phys. Rev. Lett. **101**, 127003 (2008).
 - ¹⁷ Y. Tanaka, T. Yokoyama, A. V. Balatsky, and N. Nagaosa, Phys. Rev. B **79**, 060505 (2009).
 - ¹⁸ C.-K. Lu and S. Yip, Phys. Rev. B **82**, 104501 (2010).
 - ¹⁹ P. M. R. Brydon, C. Timm, and A. P. Schnyder, New Journal of Physics **15**, 045019 (2013).
 - ²⁰ A. P. Schnyder, C. Timm, and P. M. R. Brydon, Phys. Rev. Lett. **111**, 077001 (2013).
 - ²¹ M. F. Crommie, C. P. Lutz, and D. M. Eigler, Nature **363**, 524 (1993).
 - ²² L. Capriotti, D. J. Scalapino, and R. D. Sedgewick, Phys. Rev. B **68**, 014508 (2003).
 - ²³ Q.-H. Wang and D.-H. Lee, Phys. Rev. B **67**, 020511 (2003).
 - ²⁴ H.-M. Guo and M. Franz, Phys. Rev. B **81**, 041102 (2010).
 - ²⁵ A. Akbari and P. Thalmeier, EPL (Europhysics Letters) **102**, 57008 (2013).
 - ²⁶ H. Q. Yuan, D. F. Agterberg, N. Hayashi, P. Badica, D. Vandervelde, K. Togano, M. Sigrist, and M. B. Salamon, Phys. Rev. Lett. **97**, 017006 (2006).
 - ²⁷ M. Nishiyama, Y. Inada, and G.-q. Zheng, Phys. Rev. Lett. **98**, 047002 (2007).
 - ²⁸ E. Bauer, G. Rogl, X.-Q. Chen, R. T. Khan, H. Michor, G. Hilscher, E. Royanian, K. Kumagai, D. Z. Li, Y. Y. Li, et al., Phys. Rev. B **82**, 064511 (2010).
 - ²⁹ A. B. Karki, Y. M. Xiong, I. Vekhter, D. Browne, P. W. Adams, D. P. Young, K. R. Thomas, J. Y. Chan, H. Kim, and R. Prozorov, Phys. Rev. B **82**, 064512 (2010).
 - ³⁰ B. Joshi, A. Thamizhavel, and S. Ramakrishnan, Phys. Rev. B **84**, 064518 (2011).
 - ³¹ M. Mondal, B. Joshi, S. Kumar, A. Kamlapure, S. C. Ganguli, A. Thamizhavel, S. S. Mandal, S. Ramakrishnan, and P. Raychaudhuri, Phys. Rev. B **86**, 094520 (2012).
 - ³² E. Bauer, G. Hilscher, H. Michor, C. Paul, E. W. Scheidt, A. Griboanov, Y. Seropegin, H. Noël, M. Sigrist, and P. Rogl, Phys. Rev. Lett. **92**, 027003 (2004).
 - ³³ I. Sugitani, Y. Okuda, H. Shishido, T. Yamada, A. Thamizhavel, E. Yamamoto, T. D. Matsuda, Y. Haga, T. Takeuchi, R. Settai, et al., J. Phys. Soc. Jpn. **75**, 043703 (2006).
 - ³⁴ N. Kimura, K. Ito, K. Saitoh, Y. Umeda, H. Aoki, and T. Terashima, Phys. Rev. Lett. **95**, 247004 (2005).
 - ³⁵ P. A. Frigeri, D. F. Agterberg, A. Koga, and M. Sigrist, Phys. Rev. Lett. **92**, 097001 (2004).
 - ³⁶ K. V. Samokhin, Ann. Phys. (NY) **324** (2009).
 - ³⁷ X.-L. Qi, T. L. Hughes, S. Raghu, and S.-C. Zhang, Phys. Rev. Lett. **102**, 187001 (2009).
 - ³⁸ C.-X. Liu, X.-L. Qi, H. Zhang, X. Dai, Z. Fang, and S.-C. Zhang, Phys. Rev. B **82**, 045122 (2010).
 - ³⁹ W.-Y. Shan, H.-Z. Lu, and S.-Q. Shen, New Journal of Physics **12**, 043048 (2010).
 - ⁴⁰ M. E. Peskin and D. V. Schroeder, *An Introduction to Quantum Field Theory* (Addison-Wesley New York, 1995).